



Article

Suppression of Initial Charging Torque for Electric Drive-Reconfigured On-Board Charger

Yang Xiao, Kangwei Wang *^{ORCID}, Zhi Geng *, Kai Ni ^{ORCID}, Mingdi Fan and Yong Yang

School of Rail Transportation, Soochow University, Suzhou 215131, China; yangxiao@suda.edu.cn (Y.X.); kni@suda.edu.cn (K.N.); mdfan@suda.edu.cn (M.F.); yangy1981@suda.edu.cn (Y.Y.)

* Correspondence: kwwang@suda.edu.cn (K.W.); zhigeng@suda.edu.cn (Z.G.); Tel.: +86-131-1450-2031 (K.W.); +86-151-9066-1639 (Z.G.)

Abstract: This paper presents a new electric drive-reconfigured on-board charger and initial electromagnetic torque suppression method. This proposed reconfigured on-board charger does not need many components added to the original electric drive system: only a connector is needed, which is easy to add. Specifically, the inverter for propulsion is reconfigured as a buck chopper and a conduction path to match the reconfigured windings. Two of the machine phase windings serve as inductors, while the third phase winding is reutilized as a common-mode inductor. In addition, the initial charging torque is generated at the outset of the charging process, which may cause an instant shock or even rotational movement. In order to prevent vehicle movement, the reason for the charging torque and suppression method were analyzed. Further, predictive control of the model based on mutual inductance analysis was adopted, where the charging torque was directly used as a control object in the cost function. Finally, experimental performances were applied to verify the proposed reconfigured on-board charger under constant current and constant voltage charging.

Keywords: electric drive-reconstructed onboard charger; permanent magnet motor drive; electromagnetic torque; electric vehicles



Citation: Xiao, Y.; Wang, K.; Geng, Z.; Ni, K.; Fan, M.; Yang, Y. Suppression of Initial Charging Torque for Electric Drive-Reconfigured On-Board Charger. *World Electr. Veh. J.* **2024**, *15*, 207. <https://doi.org/10.3390/wevj15050207>

Academic Editor: Aymeric Rousseau

Received: 2 April 2024

Revised: 25 April 2024

Accepted: 8 May 2024

Published: 9 May 2024



Copyright: © 2024 by the authors. Licensee MDPI, Basel, Switzerland. This article is an open access article distributed under the terms and conditions of the Creative Commons Attribution (CC BY) license (<https://creativecommons.org/licenses/by/4.0/>).

1. Introduction

The motivation of this research is to cut down the fabrication cost and increase the functions of future electric vehicles (EVs) [1–3]. Although developing a high-energy-density battery is a promising solution, it lacks, however, a technical breakthrough. It also needs to make tradeoffs regarding the cost, weight and safety [4]. Thus, one of the attractive solutions is to reconfigure the propulsive unit as an on-board battery charger. In this way, the semiconductor device, control unit, sensors, cooling system, and so on can be shared for the propulsion and charging functions [5–8].

Various types of electric drive-reconfigured on-board chargers have been proposed during the last three decades, and although electric drive-reconfigured chargers are seen as a rectifier of the on-board charger, design limitations still exist, which include AC charging torque and excessive extra components for reconfiguration. In [9], a three-phase induction motor was reused as the transformer of an on-board rectifier to charge the vehicle battery. However, an additional brake was assembled to prevent charging torque of the motor. In [10], an additional smoothing reactor was used to realize the safe charging operation for a three-phase on-board charger, which increased the complexity of its manufacture. The performance highly relied on the additional reactor as the coupled inductances among windings were not considered. In [11], a reconfigured on-board charger with a six-phase permanent magnet synchronous motor (PMSM) was proposed. The six-phase inverter served as a rectifier, while the motor windings were utilized as the filters of the rectifier. To prevent the electromagnetic torque, a phase-shifted transformer was assembled on-board, which was bulky. In [12], five-phase and seven-phase PMSM were integrated into

the reconfigured on-board charger, in which the motor windings worked as filters of the rectifier. Unfortunately, complex current rearrangement devices were installed to match the desired currents in the corresponding motor windings, which was complex and hard to implement. In [13,14], fully integrated nine-phase on-board chargers were presented. In [13], nine-phase machine windings were reutilized as filters of the grid side. Similarly, a nine-phase EV propulsive system was reconfigured as a six-phase rectifier and a three-phase buck converter for an on-board battery charger in [14]. However, the common weakness of these solutions was the overcomplicated system. Despite the possibility of these solutions in lab conditions, the nine-phase machine was far from being applied in industry. In [15], the switched reluctance machine (SRM) was reconfigured in an on-board charger, where the SRM was the central tapped type. Also, extra power switches were added in the original propulsive system, which raised new challenges in machine manufacture and circuit integration. In [16,17], SRM with open-end windings was reconfigured as an on-board charger. But the SRM was seldom adopted in EV because of the torque ripple and machine noise. In [18], a current source rectifier was used in an electric drive reconfigured charger, where motor windings were reused as filtering inductors. However, a mechanical lock was used to prevent generation of electromagnetic torque.

When the electric drive was reconfigured as the buck/boost chopper of the electric drive-reconfigured on-board charger, the electromagnetic torque turned into a DC component, which becomes convenient to analyze and suppress. In [19], an on-board charger offering electric vehicle fast charging using emerging dc distribution networks was proposed. The dual-inverter was utilized as a six-phase buck converter to achieve a high-efficiency and low-cost integrated on-board charger. In [20], a high-efficiency on-board charger was realized by using GaN and zero voltage switching. Values of 37 W/in^3 and over 96% efficiency were reached on a 6.6 kW prototype. In [21], AC machine windings were used as mutually coupled inductors to realize a double-channel interleaved boost chopper. Another idea for an isolated/bidirectional dc/dc converter in an electric drive-reconfigured on-board charger based on a PWM resonant converter was proposed in [22]. In [23], the mechanism of electromagnetic torque is presented in detail, as well as the rectifier and DC/DC converter control methods. In [24], decoupled current-balancing control (DCBC) with two parallel loops was proposed for an on-board charger. [25] investigated an electric vehicle interior permanent magnet synchronous motor (IPMSM) drive, which consisted of a double-channel interleaved bidirectional front-end dc/dc buck-boost converter and a three-phase inverter.

In summary, the challenges of the electric drive reconfigured on-board charger is the suppression of electromagnetic torque and overmuch extra components added in the electric drive system. In this manuscript, a novel electric drive reconfigured on-board charger is proposed with only one extra connector. Compared with integrated on-board chargers in [7,10], the proposed integrated charger does not use an extra inductor to improve charging performance. Instead, two of the three-phase PMSM windings serve as the inductors; meanwhile, the third motor winding is reutilized as a common-mode inductor. Thus, the ideal charging effect is achieved without adding extra inductor. Meanwhile, only by adding one power connector, the inverter for propulsion is reconfigured as a buck chopper and a conduction path to match the reconfigured motor windings. In addition, the charging torque and initial movement are discussed in this paper. To prevent the vehicle vibration during charging process, the reason of electromagnetic torque and suppression method are originally analyzed. Furthermore, the coupled phenomenon in charging of motor windings is decoupled into common-mode inductance and differential-mode inductance, which is also different from the existing literature. In addition, compared with indirect current modulation, the charging torque is directly used as a control object in the cost function of model predictive control. Finally, experimental data are given to verify the proposed reconfigured on-board charger under constant current (CC) and constant voltage (CV) charging.

2. Electric Drive Reconfigured System and Initial Charging Torque

Figure 1 demonstrates the proposed electric drive-reconfigured on-board EV charger; only a single connector K_3 is used to switch between the charging progress and the propulsive progress. Under propulsion, the connector K_1 and K_2 are on, while the K_3 is off. During the charging mode, the connector K_1 and K_2 are off, while K_3 is on. The rectifier is commonly assembled on vehicles and it is capable of unity power factor correction ability. The propulsive inverter is reused as a parallel buck chopper to produce a suitable DC voltage for the battery pack.

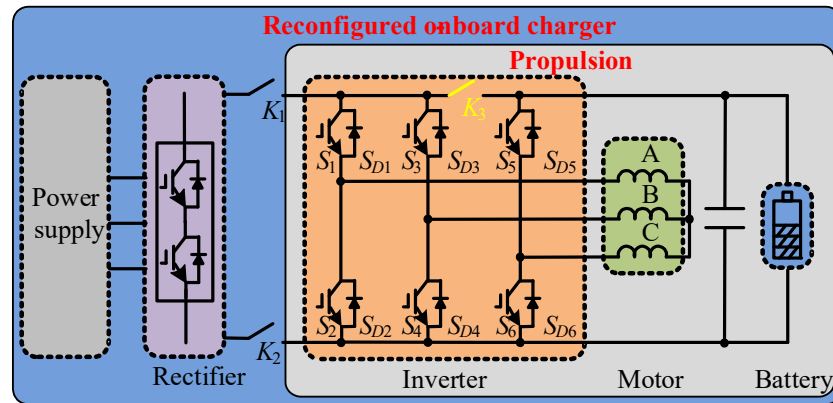


Figure 1. Electric drive reconfigured on-board charger.

The proposed electric drive reconfigured charger saves the available propulsive components and reuses them to the maximum value. First, the power switches of the inverter in the existing propulsive unit are saved by reutilizing it as a parallel buck chopper. Second, two motor windings of the PMSM are reconfigured as a parallel DC/DC inductor; meanwhile, the left phase serves as a common-mode inductor. It saves space for the battery as the inductors with high-rated current are bulky. Third, the DSP, cooling devices, and necessary hall sensors for propulsion are all reutilized in the electric drive reconfigured system. Hence, the cost and weight of the reconfigured on-board system are sharply reduced.

The expression of charging torque was derived based on the magnetic co-energy [23–26]. Thus, the charging torque in matrix form was:

$$T_e = T_{em} + T_{er} = n_p(i_s^T \psi_{fd} \frac{\partial \gamma}{\partial \theta_e} + \frac{1}{2} i_s^T \frac{\partial L_s}{\partial \theta_e} i_s) \tag{1}$$

where L_s is the matrix form of the motor inductance, $\gamma = [\cos(\theta_e) \cos(\theta_e - 2\pi/n) \dots \cos(\theta_e - 2(n-1)\pi/n)]^T$. θ_{mech} is the mechanical angle, which follows the $\theta_{mech} = \theta/n_p$. n_p is the number of pole pairs.

The inductance matrix L_s of a three-phase PMSM machine can be found in [26], including the leakage inductance L_1 , zero sequence inductance L_0 and second-order magnetizing inductance L_2 .

$$L_s = \begin{bmatrix} L_A & L_{AB} & L_{AC} \\ L_{BA} & L_B & L_{BC} \\ L_{CA} & L_{CB} & L_C \end{bmatrix} = L_1 \begin{bmatrix} 1 & 0 & 0 \\ 0 & 1 & 0 \\ 0 & 0 & 1 \end{bmatrix} + L_0 \begin{bmatrix} 1 & -0.5 & -0.5 \\ -0.5 & 1 & -0.5 \\ -0.5 & -0.5 & 1 \end{bmatrix} + L_2 \begin{bmatrix} \cos 2\theta_e & \cos 2(\theta_e - \frac{\pi}{3}) & \cos 2(\theta_e + \frac{\pi}{3}) \\ \cos 2(\theta_e - \frac{\pi}{3}) & \cos 2(\theta_e + \frac{\pi}{3}) & \cos 2\theta_e \\ \cos 2(\theta_e + \frac{\pi}{3}) & \cos 2\theta_e & \cos 2(\theta_e - \frac{\pi}{3}) \end{bmatrix} \tag{2}$$

Based on Equation (1), if the currents of every motor windings are equal to each other, for example, $i_A = i_B = i_C = I$, the electromagnetic torque will be zero. It is indicated that the motor generates no electromagnetic torque during the charging process. However, the currents in the PMSM windings in the designed reconfigure on-board charger are different;

hence, an electromagnetic charging torque, also termed as an initial charging torque, will be generated at the outset of the charging process until the electromagnetic forces are balanced. If the DC components of the motor winding currents are $i_A = i_B = I$, $i_C = -2I$, as a result, the electromagnetic torque is:

$$T_e = 3n_p I \psi_{fd} \sin(\theta_e - \pi/3) \quad (3)$$

Figure 2 shows the waveform between the electromagnetic torque and the electric rotor position. The electromagnetic torque undulates around zero and it is associated with the rotor position. Under some specific positions, the electromagnetic torque is $3n_p I \psi_{fd}$, which is close to the rated propulsive torque. Hence, the charging electromagnetic torque is unsafe and must be suppressed. Meanwhile, it was found that the electromagnetic torque does not produce at special rotor points, such as $7\pi/3$ and $13\pi/3$. These positions were named zero charging positions (ZCP). However, the ranges of ZCP may increase due to friction force and cogging torque. Hence, the ZCP areas were marked in green in Figure 2. The safe charging ranges were not the same in different motor types due to the motor inertia, friction force and cogging torque, but the ZCP areas should be around ZCP positions, such as $\pi/3$ and $4\pi/3$.

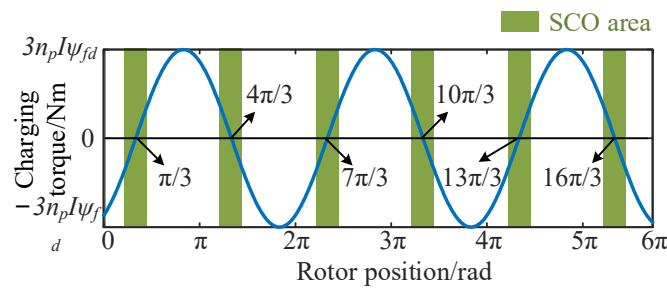


Figure 2. Electromagnetic torque at different rotor positions and ZCP area.

Moreover, the high-frequency components in motor windings will influence the generation of the initial electromagnetic torque [27]. The main high frequency components in motor winding were considered as follows:

$$\begin{cases} i_{A_high} = I_{h1} \sin(\omega t + \phi) + I_{h3} \sin(3\omega t + \phi) \\ i_{B_high} = I_{h2} \sin(\omega t + \phi) + I_{h4} \sin(3\omega t + \phi) \\ i_{C_high} = -i_{LA_high} - i_{LB_high} \end{cases} \quad (4)$$

where I_{h1} , I_{h2} , I_{h3} , and I_{h4} are the magnitudes of the current ripples, ω is the frequency of the current ripple, and ϕ is the phase position of the current ripple. The charging ripple at the safe charging position is

$$T_{er} = \frac{\sqrt{3}}{2} n_p \psi_{fd} [(I_{h1} - I_{h2}) \sin(\omega t + \phi) + (I_{h3} - I_{h4}) \sin(3\omega t + \phi)] \quad (5)$$

If the rotor does not stop at the calculated ZCPs, the machine is likely to produce enough initial electromagnetic torque to rotate the rotor, which may lead to a shock even rotational movement when the consumer is not in the vehicle. Thus, ZCP is necessary to ensure the safety of vehicles and costumers.

It also needs to be mentioned that in order to handle unexpected charging torque generation, the electric park brake was used to keep vehicle at a standstill. In addition, the charging power level was designed to ensure charging torque was small enough to limit the maximum charging torque. The encoder data were also used to detected unexpected charging torque; if unexpected charging torque occurred, the charging progress would stop immediately.

In summary, the initial electromagnetic charging torque was not equal to zero at the outset of the charging process until the rotor was at the ZCP areas. This initial movement

may have generated an instant shock on the vehicle. In addition, ripple charging torque resulting from ripples in the motor winding currents should be suppressed, because this may result in vibration and noise.

3. Initial Charging Torque Suppression

In order to maintain the rotor at the ZCP areas, the initial charging torque should be suppressed. The model predictive control was employed here to obtain the most suitable output PWM status according to the cost function [28–30]. Meanwhile, the charging torque can be set in the cost function directly compared with other indirect methods, such as the proportional integral controller.

3.1. Mutual Inductance Analysis

The model predictive control is highly reliant on the mathematic model of the charger. The strong coupling between motor windings may affect the charging performance [31]. So, the coupled inductances of motor windings were analyzed first.

The inductance of phase-C winding can provide enough common-mode inductance for good charging performance. So, only two current patterns were adopted in the electric drive reconfigured on-board charger, which is shown in Figure 3. These two current patterns were termed as Mode I and Mode II. Then, the flux of the three-phase motor was presented as

$$\psi = \begin{bmatrix} L_A & L_{AB} & L_{AC} \\ L_{BA} & L_B & L_{BC} \\ L_{CA} & L_{CB} & L_C \end{bmatrix} \begin{bmatrix} i_A \\ i_B \\ i_C \end{bmatrix} + \psi_{fd} \begin{bmatrix} \cos(\theta_e) \\ \cos(\theta_e - 2\pi/3) \\ \cos(\theta_e - 4\pi/3) \end{bmatrix} \quad (6)$$

where i_A , i_B , i_C represent the currents of three-phase motor windings; ψ_{fd} and θ_e are permanent magnet flux and electric angle. L_A , L_B and L_C are main inductances while L_{AB} , L_{BA} , L_{AC} , L_{CA} , L_{BC} and L_{CB} are mutual inductances. The relationships between mutual inductances are

$$\begin{cases} L_{AB} = L_{BA} \\ L_{AC} = L_{CA} \\ L_{BC} = L_{CB} \end{cases} \quad (7)$$

The voltages on the PMSM windings can be derived by

$$u_{ABC} = R_{ABC}i_{ABC} + \frac{d\psi_{ABC}}{dt} \quad (8)$$

$$\begin{bmatrix} u_A \\ u_B \\ u_C \end{bmatrix} = \begin{bmatrix} R_A & & \\ & R_B & \\ & & R_C \end{bmatrix} \begin{bmatrix} i_A \\ i_B \\ i_C \end{bmatrix} + \begin{bmatrix} L_A & L_{AB} & L_{AC} \\ L_{BA} & L_B & L_{BC} \\ L_{CA} & L_{CB} & L_C \end{bmatrix} \begin{bmatrix} \frac{di_A}{dt} \\ \frac{di_B}{dt} \\ \frac{di_C}{dt} \end{bmatrix}$$

where R_A , R_B , R_C are resistances of motor windings; u_A , u_B and u_C are voltages on motor windings.

The currents in motor winding are represented by differential-mode currents and common-mode currents in (9), in which i'_A and i'_B are differential-mode currents, and i_{AC} , i_{BC} and i_{CC} are common-mode currents.

$$\begin{bmatrix} i_A \\ i_B \\ i_C \end{bmatrix} = \begin{bmatrix} i'_A \\ i'_B \\ 0 \end{bmatrix} + \begin{bmatrix} i_{AC} \\ i_{BC} \\ i_{CC} \end{bmatrix} \quad (9)$$

Since the phase-C winding does not contain differential-mode current, the differential-mode currents in phase-A and phase-B are

$$i'_A + i'_B = 0 \quad (10)$$

The common-mode currents in phase-A winding and phase-B winding are

$$i_{AC} = i_{BC} = -\frac{i_{CC}}{2} \tag{11}$$

Thus, the motor phase voltages can be obtained as

$$\begin{bmatrix} u'_A \\ u'_B \end{bmatrix} = \begin{bmatrix} R_A & \\ & R_B \end{bmatrix} \begin{bmatrix} i'_A \\ i'_B \end{bmatrix} + \begin{bmatrix} L_A - L_{AB} & \\ & L_B - L_{BA} \end{bmatrix} \begin{bmatrix} \frac{di'_A}{dt} \\ \frac{di'_B}{dt} \end{bmatrix} \tag{12}$$

$$\begin{bmatrix} u_{AC} \\ u_{BC} \\ u_{CC} \end{bmatrix} = \begin{bmatrix} R_A & & \\ & R_B & \\ & & R_C \end{bmatrix} \begin{bmatrix} i_{AC} \\ i_{BC} \\ i_{CC} \end{bmatrix} + \begin{bmatrix} L_A + L_{AB} & 0 & 0 \\ -2L_{AC} & L_B + L_{BA} & 0 \\ 0 & -2L_{BC} & 0 \\ 0 & 0 & L_C - \frac{L_{AC} + L_{CB}}{2} \end{bmatrix} \begin{bmatrix} \frac{di_{AC}}{dt} \\ \frac{di_{BC}}{dt} \\ \frac{di_{CC}}{dt} \end{bmatrix} \tag{13}$$

where u'_A and u'_B represent the differential-mode voltages, while u_{AC} , u_{BC} and u_{CC} are common-mode phase voltages. The common and differential modes are summarized by the equivalent schematics in Figure 4.

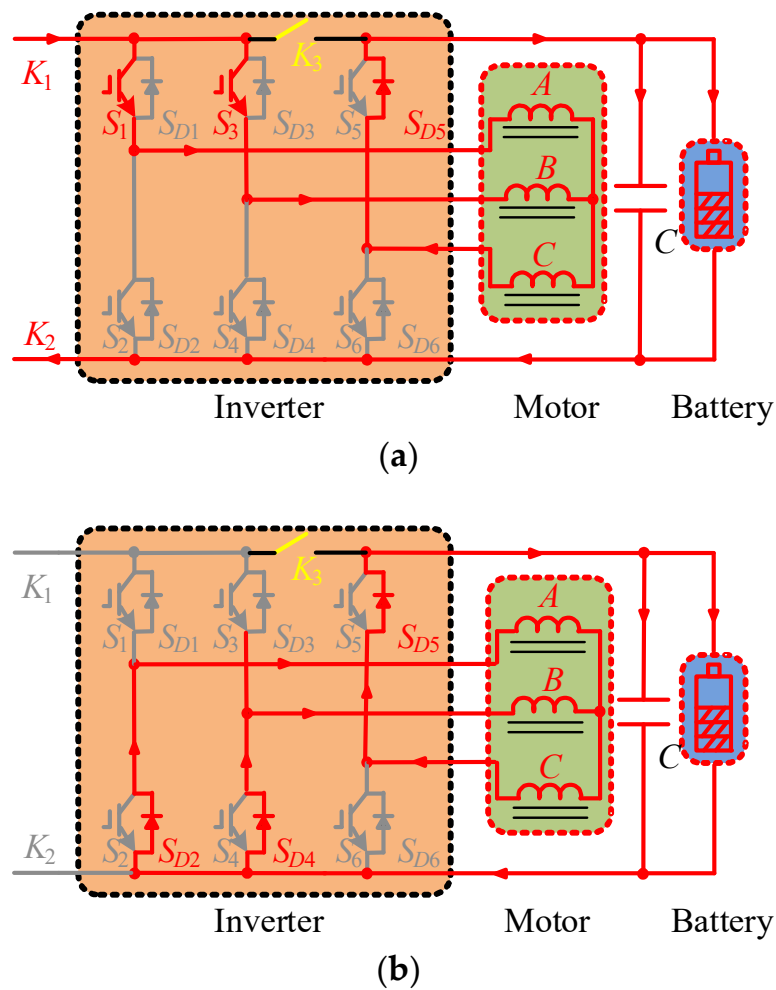


Figure 3. Current patterns of reconfigured on-board charger. (a) Mode I. (b) Mode II.

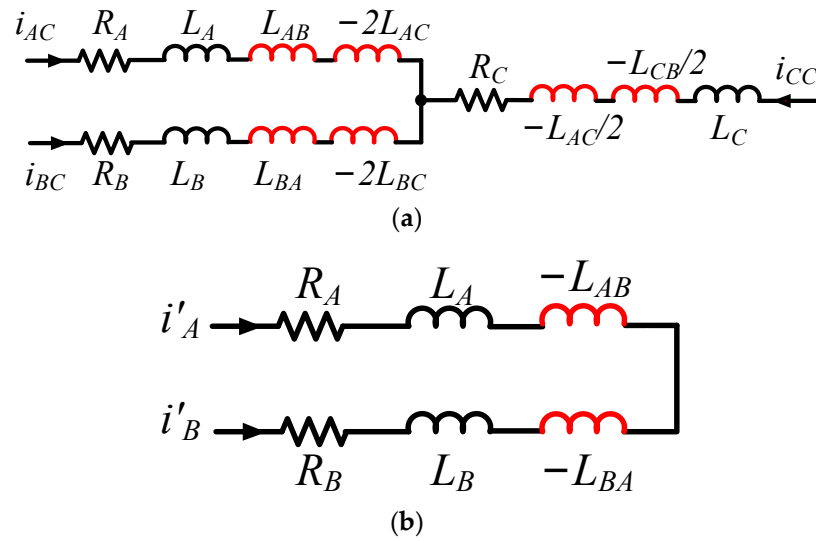


Figure 4. Common-mode and differential-mode models of the three-phase PMSM motor under charging mode. (a) Common-mode situation. (b) Differential-mode situation.

3.2. Model Predictive Control

The state equation of the electric drive-reconfigured on-board charger was obtained based on Equation (13):

$$\begin{bmatrix} \dot{i}_{AC} \\ \dot{i}_{BC} \\ \dot{i}_{CC} \end{bmatrix} = A \begin{bmatrix} i_{AC} \\ i_{BC} \\ i_{CC} \end{bmatrix} + B \begin{bmatrix} u_{AC} \\ u_{BC} \\ u_{CC} \end{bmatrix} \quad A = \begin{bmatrix} \frac{-R_A}{X} & 0 & 0 \\ 0 & \frac{-R_B}{Y} & 0 \\ 0 & 0 & \frac{-2R_C}{Z} \end{bmatrix} \quad B = \begin{bmatrix} \frac{1}{X} & & \\ & \frac{1}{Y} & \\ & & \frac{2}{Z} \end{bmatrix} \quad (14)$$

where $X = L_A + L_{AB} - 2L_{AC}$, $Y = L_B + L_{BA} - 2L_{BC}$, $Z = 2L_C - L_{AC} - L_{CB}$.

The approximate discretization model of Equation (14) at the $k + 1$ moment was obtained.

$$\begin{bmatrix} i_{AC}^{k+1} \\ i_{BC}^{k+1} \\ i_{CC}^{k+1} \end{bmatrix} = A^{k+1} \begin{bmatrix} i_{AC}^k \\ i_{BC}^k \\ i_{CC}^k \end{bmatrix} + B^{k+1} \begin{bmatrix} u_{AC}^k \\ u_{BC}^k \\ u_{CC}^k \end{bmatrix} \quad (15)$$

$$A^{k+1} = \begin{bmatrix} 1 - \frac{R_A T}{X} & 0 & 0 \\ 0 & 1 - \frac{R_B T}{Y} & 0 \\ 0 & 0 & 1 - \frac{R_C T}{Z} \end{bmatrix} \quad B^{k+1} = \begin{bmatrix} \frac{T}{X} & 0 & 0 \\ 0 & \frac{T}{Y} & 0 \\ 0 & 0 & \frac{2T}{Z} \end{bmatrix}$$

Then, the winding voltages of phase-A and phase-B at the k moment were obtained. Equation (16) is the voltages in the current pattern Mode I, while Equation (17) is in Mode II.

$$u_{AC}^k = u_{BC}^k = \frac{L_A L_B}{L_A L_B + L_C (L_A + L_B)} (U_{dc} - u_{battery}) \quad (16)$$

$$u_{AC}^k = u_{BC}^k = -\frac{L_A L_B}{L_A L_B + L_C (L_A + L_B)} u_{battery} \quad (17)$$

Next, the predictive charging torque at $k + 1$ moment is

$$T_e^{k+1} = 3n_p I^{k+1} \psi_{fd} \sin(\theta_e - \pi/3) \quad (18)$$

The control object was to reduce the charging torque to prevent potential rotor movement. So, the error function of charging torque was defined as

$$\Delta T_e = (T_e^* - T_e^{k+1})^2 \quad (19)$$

In addition, the charging status needed to be considered as the charging progress is usually divided into CC charging and CV charging. Equations (20) and (21) are the error functions in CC charging, while Equation (22) is the error function of battery voltage in CV charging. It needs to be mentioned that the battery voltage grows slowly compared with the sampling frequency, so the sampling voltage of the battery was used as the battery voltage at the $k + 1$ moment.

$$\Delta i_{AC} = (i_{AC}^* - i_{AC}^{k+1})^2 \quad (20)$$

$$\Delta i_{BC} = (i_{BC}^* - i_{BC}^{k+1})^2 \quad (21)$$

$$\Delta u_{battery} = (u_{battery}^* - u_{battery}^{k+1})^2 \quad (22)$$

Finally, the cost function in CV charging mode was defined as

$$g_{CV} = \Delta T_e + \lambda \Delta u_{battery} \quad (23)$$

The cost function in CC charging mode was defined as

$$g_{CC} = \Delta T_e + \mu (\Delta i_{AC} + \Delta i_{BC}) \quad (24)$$

where $1 > \mu > 0$ and $1 > \lambda > 0$.

The coefficient of ΔT_e was set at 1, while the coefficient of $\Delta u_{battery}$ or $(\Delta i_{AC} + \Delta i_{BC})$ is set between 0 and 1. ΔT_e affects the rotational movement of the motor during the charging process while $\Delta u_{battery}$ or $(\Delta i_{AC} + \Delta i_{BC})$ affects the charging status, such as the charging voltage and charging current. Moreover, if the coefficient of $\Delta u_{battery}$ or $(\Delta i_{AC} + \Delta i_{BC})$ is too small, vibration of motor may be produced according to Equation (5).

It needs to be mentioned that the differential-mode current in motor windings are not considered in the cost function, because the rotor position offset is acceptable only if the rotor is in the ZCP areas. Figure 5 shows the control flow chart of the model predictive control. First, the motor winding currents, encoder value, dc-link voltage and battery voltage were measured. Then, the predictive values of currents and charging torque were calculated. Afterwards, the error functions were executed based on the state of charge. Finally, the PWM codes were created according to the minimum cost function.

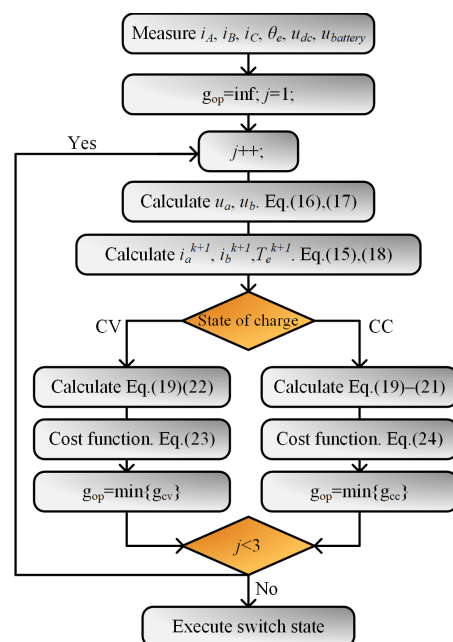


Figure 5. Control diagram of model predictive control with different state of charge.

The whole control method of the reconfigured on-board charger was divided into two parts. On the rectifier side, the unity power factor correction and output voltage control were adopted. The unity power factor correction was achieved by setting the q -axis grid current values at zero [32,33]. The output voltage control was attained by setting the value of the output voltage regulator as the reference d -axis value of the grid currents. On the reconfigured on-board charger side, the rotor was pulled to one of the ZCP areas [34,35]. Then, the model predictive control started to operate to maintain a safe charging operation and satisfy a different charging status.

4. Simulation and Experimental Results

4.1. Simulation Performance

To verify the proposed electric drive-reconfigured charger and charging operation, the simulation was first carried out in the MATLAB/SIMULINK (R2019b). It needs to be mentioned that inductances of motor winding were identified at a high frequency, which was close to the working frequency of the parallel DC/DC chopper. Also, the mutual inductances were tested at high frequency. The key parameters are listed in Table 1.

Table 1. Parameters of electric drive-reconfigured on-board charger.

Parameters	Values
Sampling frequency	150 kHz
Rated motor output	4 kW
Rated motor current	6 A
Rated rotate speed	3000 rpm
No. pole pairs	3
Phase-A winding inductance L_A	1.059 mH
Phase-A winding resistance R_A	0.482 Ω
Coupled inductance of phase AB L_{AB}	0.031 mH
Phase-B winding inductance L_B	1.001 mH
Phase-B winding resistance R_B	0.515 Ω
Coupled inductance of phase BC L_{BC}	0.062 mH
Phase-C winding inductance L_C	1.067 mH
Phase-C winding resistance R_C	0.487 Ω
Coupled inductance of phase AC L_{AC}	0.044 mH

Figure 6a exhibits the motor winding currents under 2 A CC charging with MPC. The ripple currents of the three-phase currents were 0.08 A, 0.08 A and 0.16 A. The current of phase-C was twice the currents in the other motor winding, which confirms the analysis of the electric drive-reconfigured on-board charger. Figure 6b exhibits the charging performance of the battery, motor winding current and capacitor current. The ripple current flowed through the capacitor and the charging current was stable and smooth, which ensures robust charging performance.

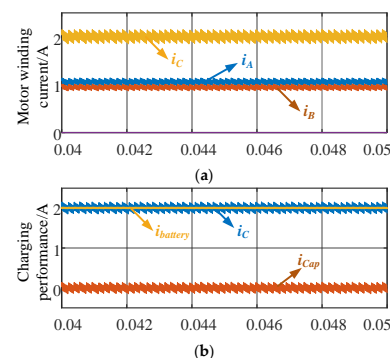


Figure 6. Simulated waveforms under CC charging with MPC. (a) Charging currents in motor windings. (b) Battery current and capacitor current.

Figure 7a exhibits the simulated results at 52 V CV charging with MPC. The current of phase-C was the sum of the currents in phase-A and phase-B, which agreed with the current distribution of the reconfigured on-board charger. Figure 7b exhibits the battery current, capacitor current and phase-C current. The ripple current did not flow through the battery, which was similar with the performance in CC charging.

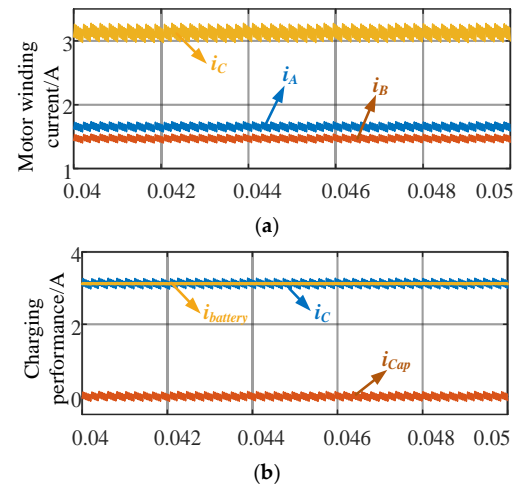


Figure 7. Simulated waveforms under CV charging with MPC. (a) Charging currents in motor windings. (b) Battery current and capacitor current.

It can be observed in both Figures 6 and 7 that differential-mode current existed, which may have generated an offset between phase-A and phase-B current. The tiny offset would not have caused rotor movement as the friction force and cogging torque may have helped to maintain the rotor in the ZCP areas.

4.2. Experimental Performance

In order to further verify the proposed reconfigured on-board charger and suppression effect, a test bed was built. Figure 8 shows the main components of the test bed, including the control desk, current probes, oscilloscope, reconfigured on-board charger, three-phase PMSM and lithium-ion battery. The reconfigured on-board charger contained an on-board charger, a set of inverters, a DSP28335, drive circuits and sampling circuits.

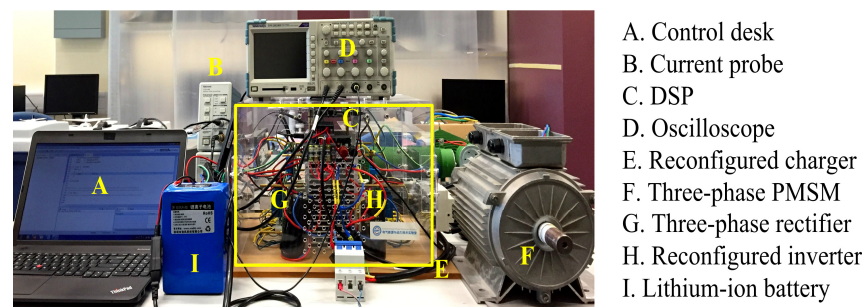


Figure 8. Testbed of proposed reconfigured on-board charger.

It also needs to be mentioned that a constant switching frequency of 5 kHz was adopted on the on-board rectifier side, while the switching frequency of the proposed on-board charger was related to the sampling frequency. In addition, the dead time on the rectifier side was 1.2 μ s, while the dead time was not used on the reconfigured side.

Figure 9 exhibits the rectifier performance of the on-board rectifier under 2 A CC charging. The transformer side voltage was 33.2 V and the dc-link voltage was set to 70 V. The rectifier currents were in the same phase as the rectifier voltage, which confirms the

unity power factor correction. The dc-link voltage was stable and had a 2 V ripple voltage, which achieved the aim of output voltage control. The total harmonic distortions of the three-phase currents were 6.72%, 6.82%, 6.88%, respectively.

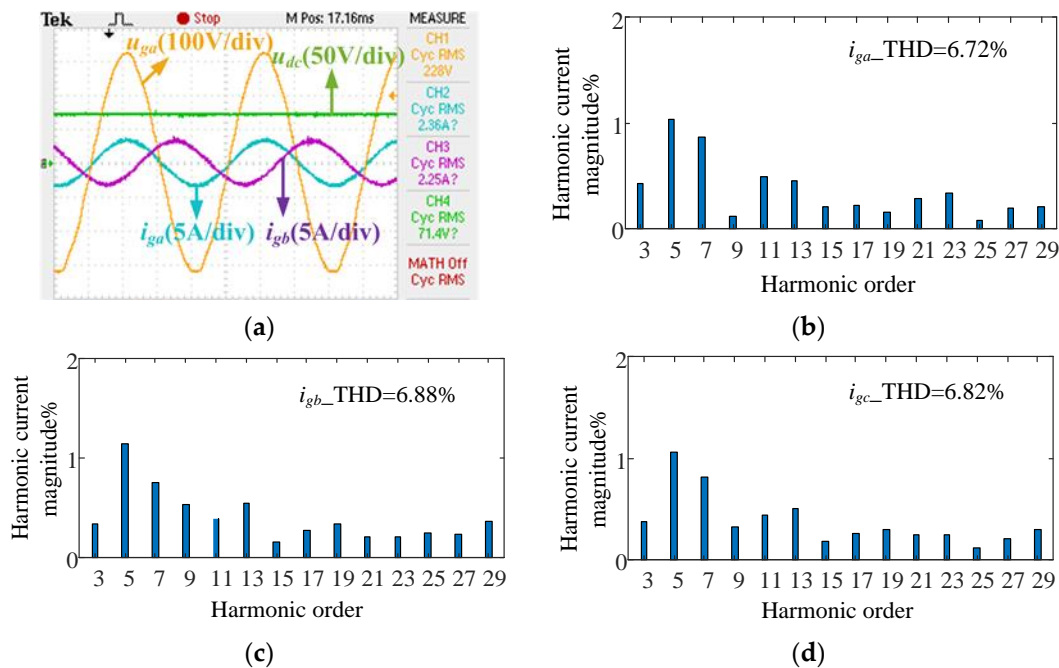


Figure 9. Grid-side performance. (a) Grid-side voltage, currents and dc-link voltage of on-board rectifier. (b) THD of i_{ga} . (c) THD of i_{gb} . (d) THD of i_{gc} .

Figure 10a exhibits the motor winding currents and battery voltage at 2 A CC charging. The instant frequencies of the ripple currents were different since predictive control was adopted. For example, the f_1 and f_2 in Figure 10a are obviously different. The ripple current performance was different from the constant frequency modulation and the average ripple frequency was about 13 kHz. In addition, the current ripples in the three-phase PMSM windings were 0.18 A, 0.18 A and 0.36 A. The differential-mode current existed in motor winding phase-A and phase-B, which confirms the mutual inductance analysis.

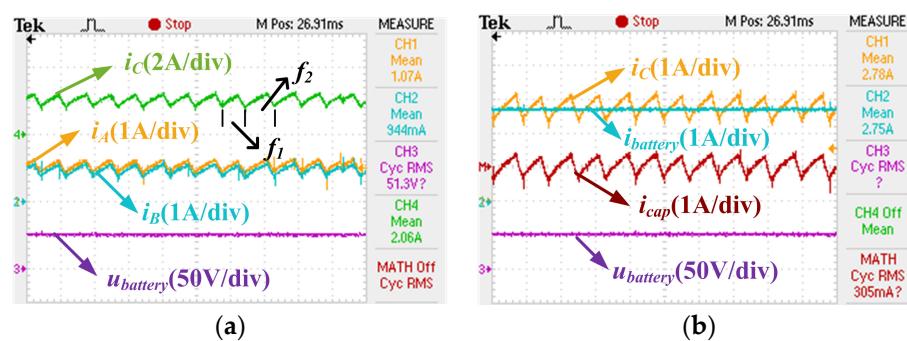


Figure 10. Experimental performance at 2 A CC charging. (a) Currents in motor windings and battery voltage. (b) Capacitor and charging currents.

Figure 10b demonstrates the battery current and capacitor current at 2 A CC charging with MPC. It was found that the current ripple in phase-C flowed through the capacitor rather than the battery. Thus, the charging current was constant and stable. Also, the battery voltage was stable under CC charging.

The amplitude of the motor winding current i_A and i_B were almost the same in CC charging mode. The motor winding current i_C was twice the motor winding current i_A and

i_B , which meets the control requirement. In addition, the motor winding currents i_A and i_B were not the same in CV charging. This is because the control object changed from current to voltage. The differential-mode current was generated due to the differential-mode inductance. The current ripple in simulation was 0.08 A, 0.08 A and 0.16 A, while the current ripple in the experiment was 0.18 A, 0.18 A and 0.36 A, which was slightly bigger than in simulation. This is because the simulation was relatively ideal, and many non-linearity elements such as power switches and battery were not accurately modeled in simulation.

Figure 11a presents the charging results under 50 V CV charging with MPC. The ripple frequency was also different from constant frequency modulation. The current ripples in the three-phase PMSM windings were 0.18 A, 0.18 A and 0.36 A. Although small imbalanced currents existed in motor winding A and motor winding B, it would not have damaged the power switches and the current stress was safe for these power switches. This is because the charging unit was reused from the inverter for propulsion and the power level of propulsion was much higher than that of charging. As a result, the current stress of charging was much lower than that of propulsion.

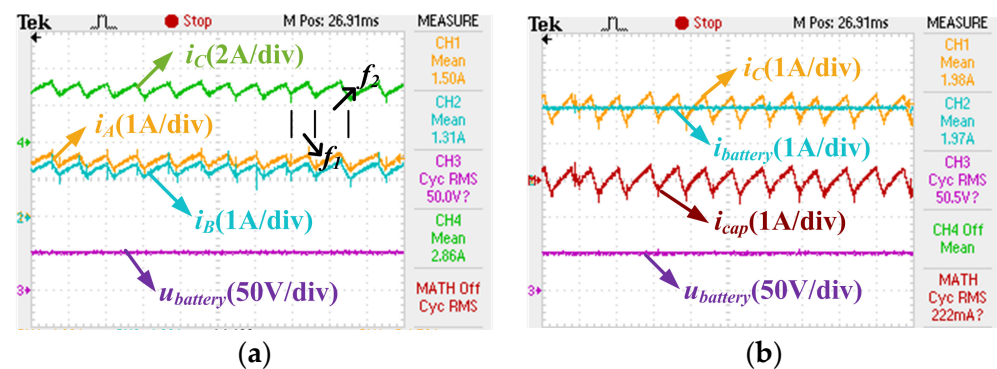


Figure 11. Experimental performance under 50 V CV charging. (a) Currents in motor windings and battery voltage. (b) Capacitor and charging currents.

Figure 11b exhibits the phase-C current, battery current and capacitor current under 50 V CV charging with MPC. The battery current was constant and the mean value was 2.75 A. The ripple current of phase-C winding flowed through the capacitor; as a result, safe and good charging performance was achieved.

Figure 12 shows the trigger wave, encoder output and charging torque without the initial charging torque suppression. The trigger wave was generated at the same moment of power on moment, so that the oscilloscope could catch the instant performance accurately. The encoder output was exported by a digital/analog converter (DAC) on the DSP, which showed the rotor movement. The charging torque was calculated by Equation (1) and was exported by DAC. Before power on moment, the encoder output was zero, which means the rotor was at the original position where phase-A was aligned with the d -axis of the machine. Meanwhile, the charging torque also stayed at zero as there was no current flow through the motor windings. When the power was on, the encoder position increased, while the charging torque stayed positive until the rotor stopped rotation. The rotor produced rotational movement and an instant shock during the power on moments, which was unsafe during the charging process. It was also observed that the electric angle of the rotational movement was 58.32° ($1.08/20 \times 360 \times 3$), which was very close to the theoretical 60° . A value of 20 is the maximum DA output of the encoder when the rotor rotates to a mechanical angle of 360. A value of 3 is the pole-pair number. The 1.68° offset was normal as the rotor still stays in the ZCP area due to friction. It should be noted that the encoder output and charging torque of ZCP were completely uniform and stable, which shows the effectiveness of initial charging torque suppression.

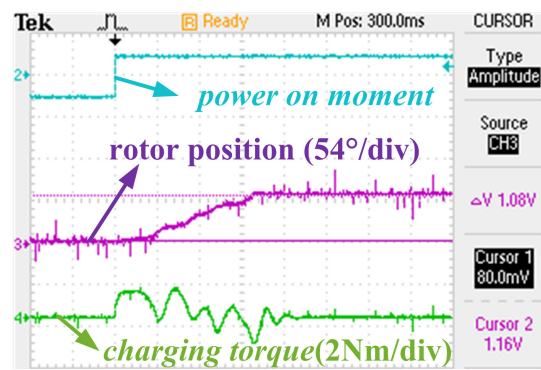


Figure 12. Charging torque and rotor position performance without initial charging torque suppression.

5. Discussion

Table 2 compares six parts with integrated on-board chargers in other studies. It was observed that all the integrated on-board chargers need connectors to separate the charging and propulsive system. In addition, most studies adopt a linear controller. The switching frequency is usually the same as the sampling frequency. However, studies have [11,13] adopted a 20 kHz sampling frequency and 10 kHz switching frequency to improve control accuracy. Since the model predictive control is adopted, sampling frequency should be much higher than the switching frequency. It needs to be mentioned that this will not add computation burden for DSP, because more advanced DSP is adopted in EVs, such as DSP 28379.

Table 2. Comparison with other works.

	Switching Frequency	Necessary Units	Power Level	Control Method	External Power Supply	Efficiency
[6]	3–5 kHz	Connectors, voltage sensors	1.5 kW	PFC, MPC	Three-phase	N/A
[7]	20 kHz	Connectors, external inductor, rectifier	1.4 kW	Phase-balance	Single-phase	<87%
[8]	20 kHz	Connectors, photovoltaic panels	1.5 kW	CC, CV	Single-phase	<90%
[10]	20 kHz	Connectors, extra inductor, rectifier	1.8 kW	CC, CV	Three-phase	<94% *
[11]	10 kHz	Connectors, phase transposition, transformer	1.1 kW	Multiple-loop	Three-phase	N/A
[13]	10 kHz	Connectors, nine-phase inverter	2.5 kW	Multi-loop	1 or 3-phase	<85%
[19]	7.5 kHz	Connectors, dual-inverter	10.35 kW	Interleaved	DC-Source	N/A
[21]	15 kHz	Connectors, diodes	3 kW	PFC, interleaved	Single-phase	93.1%
Proposed	13 kHz	Connectors, rectifier	2 kW	MPC, SCO, CC, CV	1 or 3-phase	<90%

Note: * is DC to load efficiency, others are grid to load efficiency.

Although the MPC offers good initial charging torque suppression ability, an emergency mode is suggested to avoid unexpected charging torque. The encoder needs to give feedback to detect the unexpected charging torque or movement during charging progress. If unexpected movement occurs or the primary control strategy fails, the charging progress will also stop immediately.

Since the electric drive-reconfigured on-board charger reuses the components in the propulsive system, the cost is much lower than the fully dedicated on-board charger, because at least four power switches used for DC/DC conversion and current/voltage hall sensors are saved. In addition, the efficiency of the designed charger is lower than the fully dedicated on-board charger. This is because the parameters are not very suitable for the charging system, such as the inductances and power switches. It will lead to more switching loss and ripples. Thus, the cost is lower, as well as the efficiency.

6. Conclusions

In this paper, an initial charging suppression method for the three-phase PMSM reconfigured on-board EV charger was investigated. A practical electric drive reconfigured on-board EV charger was presented, where two inverter legs for propulsion were reutilized as a parallel buck chopper, while the third leg was used as a conduction path. Also, two motor windings served as two inductors and the third winding worked as a common-mode inductor to obtain better operating performance. The rotational movement of vehicle at the beginning of the charging process was suppressed based on the analysis of charging torque. Also, universal charging torque and the corresponding safe charging operation were elaborated. Model predictive control was elaborated to suppress the initial charging torque and maintain the ZCP areas. The state of charge and charging torque were both considered directly in the cost function to offer initial charging torque suppression ability. A test rig of the proposed three-phase electric drive-reconfigured on-board charger was designed to verify the suppression effect and charging performance. Both CC charging and CV charging were achieved based on model predictive control.

Author Contributions: Conceptualization, Y.X. and Z.G.; methodology, Y.X. and K.W.; writing—original draft preparation, Y.X. and Z.G.; writing—review and editing, M.F. and Y.Y.; and visualization, K.N. All authors have read and agreed to the published version of the manuscript.

Funding: This research was funded by the Nature Science Youth Foundation of Jiangsu Province, grant number BK20220499.

Data Availability Statement: The original contributions presented in the study are included in the article, further inquiries can be directed to the corresponding authors.

Conflicts of Interest: The authors declare no conflict of interest.

References

- Williamson, S.S.; Rathore, A.K.; Musavi, F. Industrial Electronics for Electric Transportation: Current State-of-the-Art and Future Challenges. *IEEE Trans. Ind. Electron.* **2015**, *62*, 3021–3032. [[CrossRef](#)]
- De Santiago, J.; Bernhoff, H.; Ekergård, B.; Eriksson, S.; Ferhatovic, S.; Waters, R.; Leijon, M. Electrical Motor Drivelines in Commercial All-Electric Vehicles: A Review. *IEEE Trans. Veh. Technol.* **2012**, *61*, 475–484. [[CrossRef](#)]
- Liu, C.; Chau, K.T.; Wu, D.; Gao, S. Opportunities and Challenges of Vehicle-to-Home, Vehicle-to-Vehicle, and Vehicle-to-Grid Technologies. *Proc. IEEE* **2013**, *101*, 2409–2427. [[CrossRef](#)]
- Haghbin, S.; Lundmark, S.; Alakula, M.; Carlson, O. Grid-Connected Integrated Battery Chargers in Vehicle Applications: Review and New Solution. *IEEE Trans. Ind. Electron.* **2013**, *60*, 459–473. [[CrossRef](#)]
- Taha, R.A.; Abdel-Azim, W.E.; Shawier, A.; Metwly, M.Y.; Abdel-Khalik, A.S.; Hamad, M.S.; Hamdy, R.A.; Gadoue, S.; Ahmed, S. Single-Phase Charging of Six-Phase Integrated On-Board Battery Charger Using Predictive Current Control. *IEEE Trans. Transport. Electrific.* **2024**, *10*, 540–552. [[CrossRef](#)]
- Habib, A.; Shawier, A.; Abdel-Majeed, M.S.; Abdel-Khalik, A.S.; Hamad, M.S.; Hamdy, R.A.; Ahmed, S. Predictive Current Control of Six-Phase IM-Based Nonisolated Integrated On-Board Battery Charger Under Different Winding Configurations. *IEEE Trans. Power Electron.* **2022**, *37*, 8345–8358. [[CrossRef](#)]
- Kim, D.H.; Kim, M.J.; Lee, B.K. An Integrated Battery Charger with High Power Density and Efficiency for Electric Vehicles. *IEEE Trans. Power Electron.* **2017**, *32*, 4553–4565. [[CrossRef](#)]
- Yu, F.; Yin, Q.; Zhu, Z.; Cheng, X. A Multienergy Interface Electric-Drive-Reconstructed Onboard Charger for EVs with Integrated Control Strategy. *IEEE Trans. Power Electron.* **2024**, *39*, 4050–4061. [[CrossRef](#)]
- Lacressonniere, F.; Cassoret, B. Converter used as a battery charger and a motor speed controller in an industrial truck. In Proceedings of the 2005 European Conference on Power Electronics and Applications, Dresden, Germany, 11–14 September 2005; p. 7.
- Xiao, Y.; Liu, C.; Yu, F. An Integrated On-Board EV Charger with Safe Charging Operation for Three-Phase IPM Motor. *IEEE Trans. Ind. Electron.* **2019**, *66*, 7551–7560. [[CrossRef](#)]
- Subotic, I.; Bodo, N.; Levi, E.; Jones, M.; Levi, V. Isolated Chargers for EVs Incorporating Six-Phase Machines. *IEEE Trans. Ind. Electron.* **2016**, *63*, 653–664. [[CrossRef](#)]
- Subotic, I.; Bodo, N.; Levi, E. An EV Drive-Train with Integrated Fast Charging Capability. *IEEE Trans. Power Electron.* **2016**, *31*, 1461–1471. [[CrossRef](#)]
- Bodo, N.; Levi, E.; Subotic, I.; Espina, J.; Empringham, L.; Johnson, C.M. Efficiency Evaluation of Fully Integrated On-Board EV Battery Chargers with Nine-Phase Machines. *IEEE Trans. Energy Convers.* **2017**, *32*, 257–266. [[CrossRef](#)]
- Yu, F.; Zhang, W.; Shen, Y.; Mao, J. A Nine-Phase Permanent Magnet Electric-Drive-Reconstructed Onboard Charger for Electric Vehicle. *IEEE Trans. Energy Convers.* **2018**, *33*, 2091–2101. [[CrossRef](#)]

15. Hu, Y.; Song, X.; Cao, W.; Ji, B. New SR Drive with Integrated Charging Capacity for Plug-In Hybrid Electric Vehicles (PHEVs). *IEEE Trans. Ind. Electron.* **2014**, *61*, 5722–5731. [[CrossRef](#)]
16. Chang, H.; Liaw, C. Development of a Compact Switched-Reluctance Motor Drive for EV Propulsion with Voltage-Boosting and PFC Charging Capabilities. *IEEE Trans. Veh. Technol.* **2009**, *58*, 3198–3215. [[CrossRef](#)]
17. Hu, Y.; Gan, C.; Cao, W.; Li, C.; Finney, S.J. Split Converter-Fed SRM Drive for Flexible Charging in EV/HEV Applications. *IEEE Trans. Ind. Electron.* **2015**, *62*, 6085–6095. [[CrossRef](#)]
18. Shi, C.; Tang, Y.; Khaligh, A. A Three-Phase Integrated Onboard Charger for Plug-In Electric Vehicles. *IEEE Trans. Power Electron.* **2018**, *33*, 4716–4725. [[CrossRef](#)]
19. Shi, R.; Semsar, S.; Lehn, P.W. Constant Current Fast Charging of Electric Vehicles via a DC Grid Using a Dual-Inverter Drive. *IEEE Trans. Ind. Electron.* **2017**, *64*, 6940–6949. [[CrossRef](#)]
20. Liu, Z.; Li, B.; Lee, F.C.; Li, Q. High-Efficiency High-Density Critical Mode Rectifier/Inverter for WBG-Device-Based On-Board Charger. *IEEE Trans. Ind. Electron.* **2017**, *64*, 9114–9123. [[CrossRef](#)]
21. Shi, C.; Tang, Y.; Khaligh, A. A Single-Phase Integrated Onboard Battery Charger Using Propulsion System for Plug-in Electric Vehicles. *IEEE Trans. Veh. Technol.* **2017**, *66*, 10899–10910. [[CrossRef](#)]
22. Lee, B.; Kim, J.; Kim, S.; Lee, J. An Isolated/Bidirectional PWM Resonant Converter for V2G(H) EV On-Board Charger. *IEEE Trans. Veh. Technol.* **2017**, *66*, 7741–7750. [[CrossRef](#)]
23. Xiao, Y.; Liu, C. A Study of Rotational Movement and Charging Torque of Reconfigured On-Board Charger. *IEEE Trans. Power Electron.* **2020**, *35*, 10720–10728. [[CrossRef](#)]
24. Chen, H.; Lu, C.; Huang, L. Decoupled Current-Balancing Control with Single-Sensor Sampling-Current Strategy For Two-Phase Interleaved Boost-Type Converters. *IEEE Trans. Ind. Electron.* **2016**, *63*, 1507–1518. [[CrossRef](#)]
25. Lin, Y.; Hu, K.; Yeh, T.; Liaw, C. An Electric-Vehicle IPMSM Drive with Interleaved Front-End DC/DC Converter. *IEEE Trans. Veh. Technol.* **2016**, *65*, 4493–4504. [[CrossRef](#)]
26. Pellegrino, G.; Armando, E.; Guglielmi, P. An Integral Battery Charger with Power Factor Correction for Electric Scooter. *IEEE Trans. Power Electron.* **2010**, *25*, 751–759. [[CrossRef](#)]
27. Uddin, K.; Moore, A.D.; Barai, A.; Marco, J. The effects of high frequency current ripple on electric vehicle battery performance. *Appl. Energy* **2016**, *178*, 142–154. [[CrossRef](#)]
28. Zhang, Z.; Fang, H.; Gao, F.; Rodríguez, J.; Kennel, R. Multiple-Vector Model Predictive Power Control for Grid-Tied Wind Turbine System with Enhanced Steady-State Control Performance. *IEEE Trans. Ind. Electron.* **2017**, *64*, 6287–6298. [[CrossRef](#)]
29. Cortes, P.; Rodríguez, J.; Silva, C.; Flores, A. Delay Compensation in Model Predictive Current Control of a Three-Phase Inverter. *IEEE Trans. Ind. Electron.* **2012**, *59*, 1323–1325. [[CrossRef](#)]
30. Acuna, P.; Aguilera, R.P.; Ghias, A.M.Y.M.; Rivera, M.; Baier, C.R.; Agelidis, V.G. Cascade-Free Model Predictive Control for Single-Phase Grid-Connected Power Converters. *IEEE Trans. Ind. Electron.* **2017**, *64*, 285–294. [[CrossRef](#)]
31. Kim, J.; Lee, I.; Moon, G. Analysis and Design of a Hybrid-Type Converter for Optimal Conversion Efficiency in Electric Vehicle Chargers. *IEEE Trans. Ind. Electron.* **2017**, *64*, 2789–2800. [[CrossRef](#)]
32. Diab, M.S.; Elserougi, A.A.; Abdel-Khalik, A.S.; Massoud, A.M.; Ahmed, S. A Nine-Switch-Converter-Based Integrated Motor Drive and Battery Charger System for EVs Using Symmetrical Six-Phase Machines. *IEEE Trans. Ind. Electron.* **2016**, *63*, 5326–5335. [[CrossRef](#)]
33. Hou, R.; Emadi, A. A Primary Full-Integrated Active Filter Auxiliary Power Module in Electrified Vehicles with Single-Phase Onboard Chargers. *IEEE Trans. Power Electron.* **2017**, *32*, 8393–8405. [[CrossRef](#)]
34. Gulez, K.; Adam, A.A.; Pastaci, H. Torque Ripple and EMI Noise Minimization in PMSM Using Active Filter Topology and Field-Oriented Control. *IEEE Trans. Ind. Electron.* **2008**, *55*, 251–257. [[CrossRef](#)]
35. Shahnazi, R.; Shانهchi, H.M.; Pariz, N. Position Control of Induction and DC Servomotors: A Novel Adaptive Fuzzy PI Sliding Mode Control. *IEEE Trans. Energy Convers.* **2008**, *23*, 138–147. [[CrossRef](#)]

Disclaimer/Publisher’s Note: The statements, opinions and data contained in all publications are solely those of the individual author(s) and contributor(s) and not of MDPI and/or the editor(s). MDPI and/or the editor(s) disclaim responsibility for any injury to people or property resulting from any ideas, methods, instructions or products referred to in the content.